

Gyrokinetic simulations of collisionless magnetic reconnection

B. N. Rogers, S. Kobayashi, P. Ricci, W. Dorland, J. Drake et al.

Citation: *Phys. Plasmas* **14**, 092110 (2007); doi: 10.1063/1.2774003

View online: <http://dx.doi.org/10.1063/1.2774003>

View Table of Contents: <http://pop.aip.org/resource/1/PHPAEN/v14/i9>

Published by the [American Institute of Physics](#).

Related Articles

Morphology and dynamics of three interacting kink-unstable flux ropes in a laboratory magnetoplasma
Phys. Plasmas **19**, 102102 (2012)

Magnetic reconnection in space
Phys. Plasmas **19**, 092902 (2012)

Spectroscopic observation of simultaneous bi-directional reconnection outflows in a laboratory plasma
Phys. Plasmas **19**, 080704 (2012)

The role of compressibility in energy release by magnetic reconnection
Phys. Plasmas **19**, 082109 (2012)

Design of a dual sensor probe array for internal field measurement in Versatile Experiment Spherical Torus
Rev. Sci. Instrum. **83**, 10D721 (2012)

Additional information on *Phys. Plasmas*

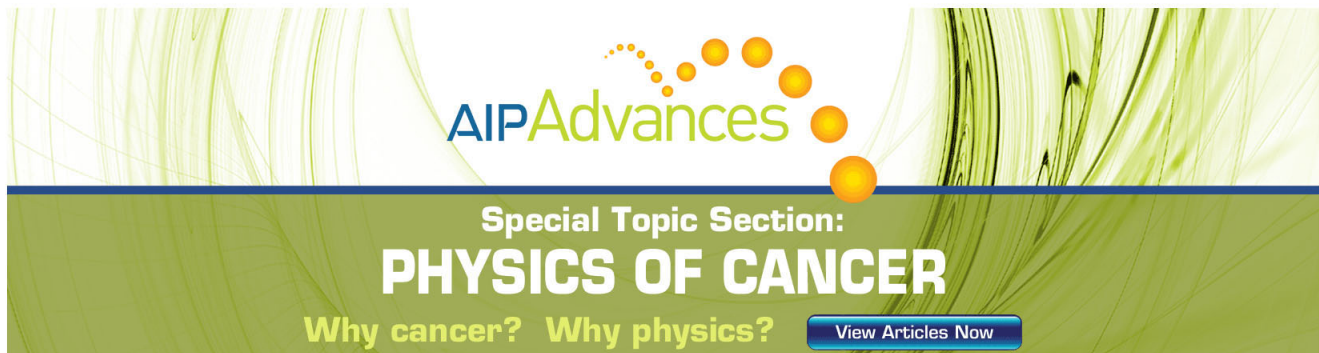
Journal Homepage: <http://pop.aip.org/>

Journal Information: http://pop.aip.org/about/about_the_journal

Top downloads: http://pop.aip.org/features/most_downloaded

Information for Authors: <http://pop.aip.org/authors>

ADVERTISEMENT



AIP Advances

Special Topic Section:
PHYSICS OF CANCER

Why cancer? Why physics? [View Articles Now](#)

Gyrokinetic simulations of collisionless magnetic reconnection

B. N. Rogers^{a)} and S. Kobayashi

Department of Physics and Astronomy, Dartmouth College, Hanover, New Hampshire 03755, USA

P. Ricci

Centre de Recherches en Physique des Plasmas, École Polytechnique Fédérale de Lausanne, Association EURATOM-Confédération Suisse, CH-1015 Lausanne, Switzerland

W. Dorland, J. Drake, and T. Tatsuno

University of Maryland, College Park, Maryland 20742, USA

(Received 3 July 2007; accepted 27 July 2007; published online 20 September 2007)

Linear and nonlinear gyrokinetic simulations of collisionless magnetic reconnection in the presence of a strong guide field are presented. A periodic slab system is considered with a sinusoidally varying reconnecting magnetic field component. The linear growth rates of the tearing mode in both the large and small Δ' regimes are compared to kinetic and fluid theory calculations. In the nonlinear regime, focusing on the limit of large Δ' , the nonlinear reconnection rates in the gyrokinetic simulations are found to be comparable to those obtained from a two-fluid model. In contrast to the fluid system, however, for $T_i \gg T_e$ and very small initial perturbation amplitudes, the reconnection in the gyrokinetic system saturates in the early nonlinear phase. This saturation can be overcome if the simulation is seeded initially with sufficient random noise. © 2007 American Institute of Physics. [DOI: 10.1063/1.2774003]

I. INTRODUCTION

We present linear and nonlinear gyrokinetic simulations of collisionless magnetic reconnection in the presence of a strong guide field. Our simulations are based on the GS2 code,^{1,2} which time evolves the nonlinear electromagnetic gyrokinetic equations³ for both electrons and ions. These equations, together with Maxwell's equations, govern the evolution of the electron and ion distribution functions (depending here on 2 spatial and 2 velocity-space coordinates) and the self-consistent electric and magnetic fields. A summary of the full system of equations is given in Appendix A.

The GS2 formalism is based on the reduced magnetohydrodynamic (MHD) ordering (see, e.g., Ref. 4), in which the deviations of the absolute levels of the density, temperatures, and the magnetic field (for example) are assumed to be small over the region of interest, though deviations in the gradients of these quantities can be comparable to or larger than the equilibrium values. Such an ordering is appropriate to the study of strong guide field reconnection, in which the component of the magnetic field that reconnects is small compared to the total magnetic field strength. The magnetic field and plasma profile variations associated with reconnection in this case, even in the nonlinear phase, are small compared to the unperturbed background values. Similarly, the time variations associated with reconnection in the large guide-field regime are slow compared to the ion gyroperiod. These properties are both necessary for the gyrokinetic approach, in which one of the three velocity-space coordinates (present in a full Vlasov treatment, for example) is eliminated from the system by a gyroangle average. This is computationally an advantage relative to full-particle simulations because it

avoids the necessity to time-resolve the gyroperiod of the particles, which in the strong guide field limit is much faster than the time scale on which the modes of interest evolve. A similar computational gain is made in GS2 by enforcing total pressure balance, which eliminates compressional magneto-sonic waves from the system while preserving the shear-Alfvén dynamics that are essential to reconnection.

We consider a collisionless periodic slab geometry with a sinusoidally varying reconnecting magnetic field component $B_y(x) \propto \sin(k_x x)$. Depending on the dominant wavelength of the tearing mode under consideration (i.e., $k_y = 2\pi/L_y$, where L_y is the length of the system in the y -direction), this system allows us to explore reconnection in either the limits of large Δ' (relevant to the $m=1$ mode in tokamaks, for example, or the GEM Reconnection Challenge Project⁵) or small Δ' (relevant to tokamak tearing modes with $m > 1$). We focus on a parameter regime of interest to magnetic confinement fusion experiments in which $\rho_s > d_e$, where $\rho_s = c_s/\Omega_{ci}$ is the ion sound Larmor radius, $d_e = c/\omega_{pe}$ is the collisionless electron skin depth, $\omega_{pe}^2 = 4\pi n e^2/m_e$, $c_s^2 = (T_i + T_e)/m_i$, $\Omega_{ci} = eB/(m_i c)$. Both the linear and nonlinear regimes are considered. In the linear case, we compare the gyrokinetic growth rates to analytical and numerical calculations based on kinetic and two-fluid models. Although reasonably good agreement between the two is found in some cases (small T_i/T_e and low β), some of the parameters explored here ($T_i \gtrsim T_e$ and $\beta \sim 1$) fall in a regime in which existing analytic calculations are not clearly reliable. A rigorous treatment of these cases would seem to require the full gyrokinetic model and include, among other things, both electron and ion finite Larmor radius (FLR) effects. Although such an analysis is beyond the scope of the present article, derivations of some of the analytic results to which we com-

^{a)}Electronic mail: barrett.rogers@dartmouth.edu

pare are given in Appendix B, and the problems with these calculations are discussed.

In the nonlinear regime, we focus on a large- Δ' case that corresponds approximately to the fastest-growing linear mode evolved into the nonlinear regime. We find the reconnection rates in the gyrokinetic system are comparable to those obtained from simulations based on a two-fluid model. An exception arises for $T_i \gg T_e$ and very small initial perturbation amplitudes, in which the nonlinear growth of the mode in the gyrokinetic system saturates in the early nonlinear phase (island widths comparable to ρ_i). This saturation can be overcome if small-amplitude random noise is added to the initial configuration.

The results discussed in this paper build on a number of other gyrokinetic studies of linear and nonlinear reconnection. Reference 6 applies gyrokinetic particle simulations to the study small-scale magnetic islands (widths comparable to the electron skin depth $d_e = c/\omega_{pe}$) in the presence of a narrow (about $10d_e$) current sheet. References 7 and 8 explore reconnection in the small Δ' case with gyrokinetic ions and drift-kinetic electrons. In larger box sizes ($\sim 64\rho_i$) an instability with odd parity was found to dominate the system, in contrast to the expected even parity of the tearing mode. In the large Δ' nonlinear simulations described here, such odd-parity modes have not been observed.

This paper is organized as follows: In Sec. II we describe the initial equilibrium and numerical simulation model. In Sec. III we compare the GS2 simulation results to linear theory calculations. We turn to the nonlinear regime in Sec. IV, in which we address the reconnection rate and saturation behavior. Our main conclusions are summarized in Sec. V. The gyrokinetic equations used in the simulations are described in Appendix A, and the derivations of various linear theory results are given in Appendix B.

II. INITIAL EQUILIBRIUM AND SIMULATION MODEL

The initial, unperturbed equilibrium state we consider is given by

$$\vec{B} = B_{z0}\hat{z} + B_{y0}(x)\hat{y}, \quad B_{y0}(x) = B_{y0\max} \sin(k_x x), \quad B_{z0} \gg B_{y0}, \quad (1)$$

$$n = n_0 = \text{const}, \quad T_i = T_{i0} = \text{const}, \quad T_e = T_{e0} = \text{const}. \quad (2)$$

For most of the numerical simulations discussed in this work we take $k_x \rho_{se} = 0.2$ (equivalent to a box size of $L_x = 2\pi/k_x = 10\pi\rho_{se}$), where

$$\rho_{se} = \frac{c_{se}}{\Omega_{ci}} = \sqrt{\frac{T_e}{m_i}} \frac{m_i c}{e B_{z0}} = \sqrt{\frac{\beta_e}{2}} d_i, \quad (3)$$

$$d_i^2 = \frac{c^2}{\omega_{pi}^2} = \frac{c^2 m_i}{4\pi n_0 e^2},$$

$$\beta_e = \frac{8\pi n_0 T_e}{B_{z0}^2}.$$

Other definitions that will be used later include

$$\rho_s^2 = (1 + T_i/T_e)\rho_{se}^2 = \frac{\beta}{2} d_i^2,$$

$$\beta = \frac{8\pi n_0 (T_i + T_e)}{B_{z0}^2}, \quad (4)$$

$$d_e^2 = \frac{c^2}{\omega_{pe}^2} = \frac{m_e}{m_i} d_i^2.$$

Note that ρ_{se} is the ion sound Larmor radius based on T_e while ρ_s is based on $T_e + T_i$.

A summary of the gyrokinetic and Maxwell equations solved by the GS2 code is given in Appendix A. The temporal discretization in GS2 to solve the linear terms in these equations is implicit and second order accurate in time. Nonlinearities are evaluated using an explicit Adams-Bashforth time-stepping scheme. In the x and y directions (the 2D plane of reconnection simulated here) a dealiased pseudospectral algorithm is used. In the x -direction the simulations include n_x Fourier modes with $64 \leq n_x \leq 8192$, depending on parameters. In the y direction the nonlinear runs have a box size $L_y = 2.5L_x = 25\pi\rho_{se}$ (corresponding to $k_{y,\min}\rho_{se} = 0.08$) and $64 \leq n_y \leq 256$. The grid points in velocity space are chosen using Gaussian integration rules. Typical runs include 16 grid points in the particle (ion or electron) energies $\epsilon_\alpha = m_\alpha v_\alpha^2/2$ in the velocity range $0 \leq v_\alpha \leq 6v_{th\alpha}$, and 10 points in $\xi_\alpha = v_{\parallel\alpha}/v_\alpha$. The simulations within this range appear to be well converged and show little dependence on the velocity-space resolution. As discussed later, to facilitate parameter scans using modest numerical resources, an artificial electron to ion mass ratio is used, either $m_e/m_i = 1/25$ or $m_e/m_i = 1/100$.

III. LINEAR REGIME

The simulations described in this section address two main cases

$$\text{Case I: } k_x \rho_{se} = 0.2, \quad m_i/m_e = 100, \quad \beta_e = 0.2,$$

$$T_i/T_e = (2.0 \times 10^{-4}, 5), \quad (5)$$

$$\text{Case II: } k_x \rho_{se} = 0.2, \quad m_i/m_e = 25, \quad \beta_e = 0.3,$$

$$T_i/T_e = (2.0 \times 10^{-5}, 5). \quad (6)$$

The simulation results in cases I and II are shown in Figs. 1 and 2, respectively. The black “+” symbols denote the GS2 values for very small $T_i/T_e \ll 1$ and the blue triangles represent $T_i/T_e = 5$. Simulations at $T_i/T_e = 1$ (not shown) are intermediate between the two, indicating the gyrokinetic growth rates (though not the eigenmode structure, as we show later) are only very weakly dependent on T_i/T_e . Since β_e is held fixed in both cases, this is equivalent to an insensitivity to either the ion β_i or the total plasma β , which for the parameters of case II, for example, varies from $\beta = 0.3$ for $T_i/T_e \approx 0$ to $\beta = 1.8$ for $T_i/T_e = 5$. Both cases I and II satisfy the inequality $\rho_s^2 \gg d_e^2$ (equivalent to $\beta \gg 2m_e/m_i$), which, aside from being relevant to fusion devices, is required to allow comparison to some analytic calculations discussed below.

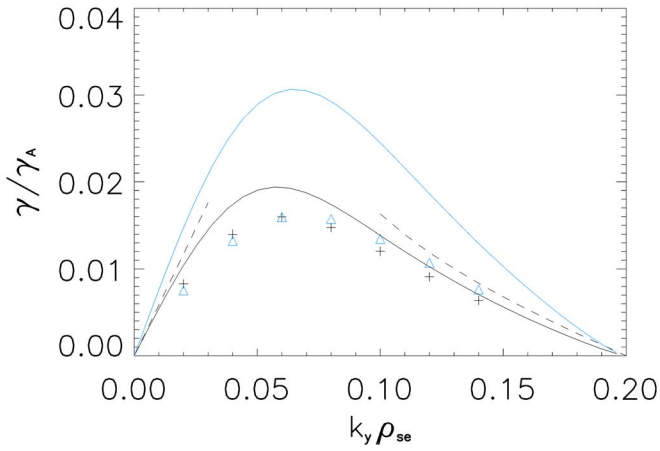


FIG. 1. (Color online) Linear growth rates γ/γ_A vs $k_y \rho_{se}$ for case I with γ_A given by Eq. (10) and $\rho_{se} = c_{se}/\Omega_{ci}$. The “+” are GS2 values for $T_i/T_e \ll 1$, triangles $T_i/T_e = 5$. The left and right dashed lines are Eqs. (10) and (11), respectively, with $T_i = 0$. The solid lines are the numerical solution of a reduced four-field fluid model for $T_i = 0$ (lower) and $T_i = 5T_e$ (upper).

These analytic results are shown in Figs. 1 and 2 as the dashed and solid lines.

Numerical convergence tests have been carried out across the full range of k_y . The spatial resolution requirements in the x -direction for convergence of the growth rates in the smaller- k_y regime are modest ($n_x \sim 64$ for $k_y \rho_{se} = 0.08$ and $m_i/m_e = 25$) but increase strongly as k_y is increased ($n_x \sim 8192$ for $k_y \rho_{se} = 0.16$ and $m_i/m_e = 100$). Such fine resolution levels in turn lead to severe time-step restrictions. Consistent with the observed trend in the resolution, the linear theory calculations discussed later suggest the tearing layer becomes narrower as k_y is increased. The number of modes required at higher k_y exceeds what one might expect from simple estimates, however, and is still under study.

The k_y dependence of γ seen in Figs. 1 and 2 is governed by the tearing mode stability parameter Δ' .⁹ This parameter may be defined in terms of \tilde{B}_x , the x -component of the magnetic field perturbation in the ideal regions outside the

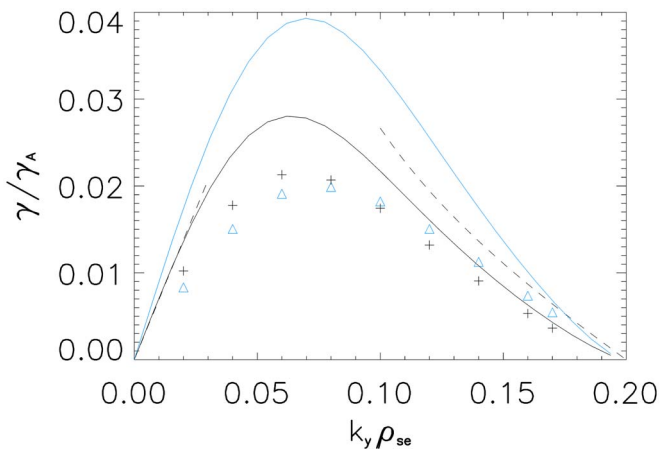


FIG. 2. (Color online) Linear growth rates for case II with the same notation as Fig. 1.

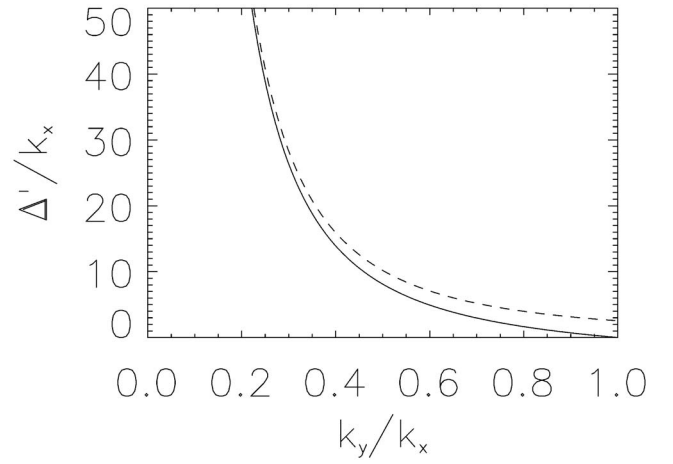


FIG. 3. Δ'/k_x given by Eq. (8) vs k_y/k_x .

tearing layer. In our system, considering the layer at $x=0$ (see, e.g., Ref. 10),

$$\tilde{B}_x \propto \cos[D(k_x|x| - \pi/2)] \sin(k_y y), \quad D \equiv \sqrt{1 - (k_y/k_x)^2} \quad (7)$$

where k_y is the wavenumber of the linear mode of interest, and

$$\Delta' = \left[\frac{\partial_x \tilde{B}_x}{\tilde{B}_x} \right]_{x=0-}^{x=0+} = 2k_x D \tan(\pi D/2). \quad (8)$$

A plot of Δ'/k_x is shown in Fig. 3 as a function of k_y/k_x (solid curve). Consistent with Figs. 1 and 2 tearing modes are unstable in the regime $k_y < k_x$ (here, $k_y \rho_{se} < 0.2$) in which $\Delta' > 0$. For $k_y \ll k_x$, $\Delta'/k_x \approx 8k_x^2/(\pi k_y^2) \gg 1$ (dashed curve). The small- Δ' regime lies to the right of the peak γ values in Figs. 1 and 2; in this regime Δ' is sufficiently small so that the constant- ψ approximation is valid across the tearing layer. The large- Δ' regime includes the peak growth rates as well as the regions to the left of the peaks in which the growth rates increase (at these parameters) linearly with k_y . The k_y value of the peak growth rate and the corresponding value of Δ' can be estimated, for example, by balancing the expression for γ that applies to the left of the peak [in the large- Δ' regime; see Eq. (10)] with the expression for γ that applies to the right of the peak [in the small- Δ' regime; see Eq. (11)]. This yields

$$\Delta'_{\max} \approx 2^{1/3} \pi^{2/3} \rho_s^{-1/3} d_e^{-2/3}. \quad (9)$$

For the parameters of cases I and II this reduces to $\Delta'_{\max} \approx 28$ and $\Delta'_{\max} \approx 20$, respectively, or (with Fig. 3 and $k_x \rho_{se} = 0.2$), $k_y \rho_{se} \approx 0.06$ for either case, consistent with the location of the peaks in Figs. 1 and 2.

A. Large Δ'

In the regime $\rho_s > d_e$ under consideration, various analytic results have been obtained in the limits of both large and small Δ' . At large Δ' , the analytic results typically apply in the regions to the left of the peak growth rates in Figs. 1 and 2 where $\gamma \propto k_y$. The expression for γ obtained in Ref. 10, for example, is given by

$$\gamma = \left(\frac{2}{\pi}\right)^{1/3} k_y d_e^{1/3} \rho_s^{2/3} \gamma_A, \quad (10)$$

$$\gamma_A = \frac{1}{\sqrt{4\pi n_0 m_i}} \left[\frac{dB_{y0}}{dx} \right]_{x=0} = \frac{k_x B_{y0 \max}}{\sqrt{4\pi n_0 m_i}}.$$

This result was obtained in Ref. 10 using an isothermal fluid electron model and an ion model that includes leading-order FLR effects for arbitrary T_i/T_e but ignores sound-wave coupling under the assumption $\gamma \gg k_{\parallel c_s}$. [A similar result, smaller than Eq. (10) by a factor of $\sqrt{2/\pi}^{1/6} \approx 1.17$, was also obtained in Ref. 11 for $T_i \ll T_e$.] For convenience, a derivation of Eq. (10) is given in Appendix B, where we also show that a drift-kinetic electron treatment (along with a Padé approximation to the electron plasma dispersion function) gives the same result as the isothermal fluid electron model used in Ref. 10. In the case of $T_i \ll T_e$ Eq. (10), shown as dashed lines on the left-hand sides of Figs. 1 and 2, agrees reasonably well with the gyrokinetic results. As we discuss in more detail later, for small k_y Eq. (10) is also approximately equivalent to an isothermal two-fluid model result shown as the upper ($T_i/T_e=5$) and lower ($T_i/T_e=0$) solid curves. These curves were obtained by solving numerically a set of four coupled reduced fluid equations described in Ref. 12, which go beyond Eq. (10) to allow for ion sound wave coupling and arbitrary β , but are formally valid only for $T_i \ll T_e$. These curves are also essentially indistinguishable from a numerical solution (not shown) of the full, nonreduced two-fluid model that is discussed in Sec. IV. To generate the upper ($T_i/T_e=5$) solid curves in the figures, we have incorporated finite T_i effects into the fluid model of Ref. 12 by the replacement $T_e \rightarrow T_e + T_i$. This is equivalent to assuming isothermal ion and electron equations of state and is consistent with the T_i/T_e dependencies of Eqs. (10) and (11). It is not, however, consistent with the gyrokinetic growth rates, which for our parameters show a much weaker dependence on T_i/T_e . Indeed, at large Δ' the analytic and fluid model growth rates increase with T_i/T_e while the gyrokinetic results display the opposite trend.

B. Small Δ'

Turning now to the case of small Δ' , the dashed lines on the right-hand sides of Figs. 1 and 2 show the following asymptotic result of Refs. 10 and 13 evaluated at $T_i=0$:

$$\gamma = \frac{1}{\pi} k_y \rho_s \gamma_A d_e \Delta'. \quad (11)$$

Like Eq. (10), for convenience this expression is derived in Appendix B from a kinetic ion treatment and either an isothermal drift-kinetic or fluid electron model. A similar result

was also obtained in Refs. 14 and 15, aside from the replacement $\rho_s \rightarrow \rho_{se}$ and an overall factor of $\sqrt{\pi}/2 \approx 1.13$. The GS2 results indicate that γ increases much more weakly with T_i/T_e than either Eq. (11) or the two-fluid model. We note that earlier versions of the two fluid model^{16,17} that neglected the electron gyroviscous terms in the electron momentum equation show much poorer agreement with the gyrokinetic simulations in the collisionless small- Δ' limit.

C. Limitations of the analytic and fluid model results

The analytic and fluid model results shown in Figs. 1 and 2 rely on some simplifying assumptions that are not clearly valid in our parameter regime. As we now explain, a simple isothermal or adiabatic equation of state cannot be strictly correct in both the innermost electron layer where $\gamma \gtrsim k_{\parallel} v_{the}$ and the outermost zone in which $\gamma \ll k_{\parallel} v_{the}$ [note $k_{\parallel} = k_y B_y(x)/B \approx k'_{\parallel} x$ is x -dependent within the tearing layer; see Eq. (B3)]. Similarly, the nongyrokinetic calculations neglect electron FLR effects, the electron polarization drift, and ion sound wave coupling (the fluid model includes the latter but only in the zero-ion-FLR limit); all effects that, for $T_i \sim T_e$, become non-negligible at essentially the same point. Since ion FLR and finite- β effects at $T_i=5T_e$ are also non-negligible, reliable analytic calculations in our higher- T_i parameter regime are thus a formidable challenge and have yet to be carried out.

Electron FLR effects are potentially important because the electron motion [see, e.g., the expression for the current density given by Eq. (B15)], for either large or small Δ' , varies on the scale length

$$\delta = \frac{\gamma}{k'_{\parallel} v_{th}} = \frac{\gamma d_e}{k_y \rho_s \gamma_A}, \quad v_{th} = \sqrt{\frac{T_e + T_i}{m_e}}. \quad (12)$$

The neglect of electron FLR effects requires that this scale, which at large Δ' is a weakly decreasing function of T_i/T_e , exceed ρ_e ; a condition that for the parameters of cases I and II and large Δ' is marginally satisfied at $T_i=0$ but is violated at $T_i/T_e=5$. Similarly, at $T_i/T_e > 1$, E_{\parallel} and ϕ also exhibits fine-scale structure for $x \sim \delta$ [see Eq. (B21)]:

$$E_{\parallel} \approx E_{\parallel}(0) \left(\frac{\delta^2 + \frac{T_e}{T_e + T_i} x^2}{\delta^2 + x^2} \right). \quad (13)$$

This expression, similar to the behavior noted in Ref. 18, predicts that E_{\parallel} for $T_i/T_e > 1$ drops by a factor of $T_e/(T_e + T_i)$ on the δ scale. For larger $x \gg \delta$ [see Eq. (B22)] E_{\parallel} then decays to zero on the ρ_s scale. The consistency of this with the simulations can be seen in Fig. 4, which shows $E_{\parallel}/E_{\parallel}(0)$ in the linear regime for the case II parameters at $k_y \rho_{se} = 0.05$ (large Δ'). The width of the narrow peak at $x=0$ for $T_i/T_e=5$ (solid line) is comparable to ρ_e and is broader than δ , consistent with the expectation that ρ_e effects are becoming important. At $T_i \ll T_e$ (dashed line), such fine-scale structure is absent as expected from Eq. (13).

A related effect, which only becomes important at finite T_i/T_e , is the electron polarization drift [see Eqs. (B30) or (B33)],

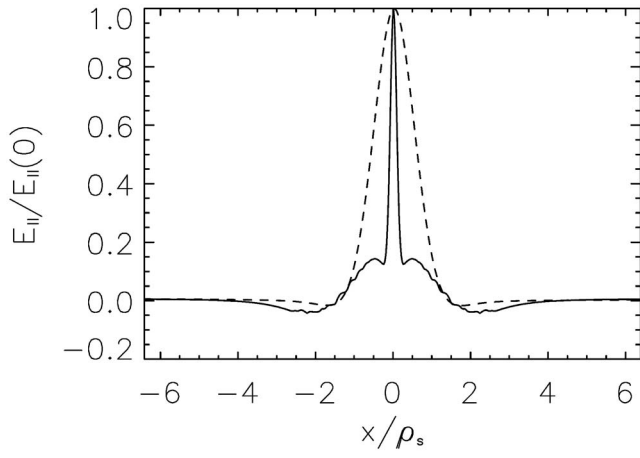


FIG. 4. $E_{\parallel}/E_{\parallel}(0)$ for case II with $k_y \rho_{se}=0.05$ and $T_i/T_e=5$ (solid), $T_i/T_e=2 \times 10^{-5}$ (dashed). Sub- ρ_s structure appears only for $T_i/T_e \sim 1$ or larger.

$$\tilde{n}_{e,\text{pol}} \sim -\frac{n_0 e}{T_e} \rho_e^2 \nabla^2 \phi. \quad (14)$$

When $k_{\perp} \rho_i \ll 1$ and the ions are magnetized, the contribution of $\tilde{n}_{e,\text{pol}}$ is negligible compared to the ion polarization drift. At finite T_i , however, the ion response for $x \sim \delta \ll \rho_i$ becomes adiabatic [see Eq. (B1), neglecting Γ_0],

$$\tilde{n}_i \sim -\frac{n_0 e}{T_i} \phi. \quad (15)$$

Estimating $\nabla^2 \phi \sim \phi/\delta^2$, the contribution of Eq. (14) is found to be negligible compared to Eq. (15) when $(T_i/T_e)\rho_e^2 \ll \delta^2$. This condition may be combined with the electron FLR restriction $\rho_e^2 \ll \delta^2$ to yield

$$\frac{(1+T_i/T_e)\rho_e^2}{\delta^2} = \frac{\beta k_y^2 \rho_s^2 \gamma_A^2}{2 \gamma^2} \ll 1. \quad (16)$$

Again, at large Δ' , this condition for the case I and II parameters is marginally satisfied at $T_i \ll T_e$ but is violated for $T_i/T_e=5$. With the expression for γ given by Eq. (10), it may also be written as $\beta/2 < (m_e/m_i)^{1/4}$, a condition that was also emphasized in Refs. 16 and 17. Due to the k_y^2 factor in the numerator, Eq. (16) is even more difficult to satisfy at small Δ' (large k_y) than at large Δ' (small k_y). Thus, even for $T_i \ll T_e$, we would expect electron FLR effects—absent in Eq. (11) and the two-fluid model—to play an even greater role.

Two other effects absent from Eqs. (10) and (11), (though not the two-fluid curves) are contributions from \tilde{B}_{\parallel} , which become potentially significant for $T_i=5T_e$ where $\beta \sim 1$, as well as ion sound wave coupling, which may be neglected only if $\gamma^2 \gg k_{\parallel}^2 c_s^2$ for $x \leq \rho_s$ [the outer envelope of the ion response, see Eq. (B18)]. Given $k_{\parallel}=k'_{\parallel}x$ this condition may be written as $\gamma^2 \gg k_{\parallel}^2 \rho_s^2 c_s^2$ or, since $\rho_s^2 c_s^2 = (1+T_i/T_e)\rho_e^2 v_{\text{th}}^2$, $\gamma^2 \gg k_{\parallel}^2 v_{\text{th}}^2 (1+T_i/T_e)\rho_e^2$. In the latter form, recalling that $\delta^2 = \gamma^2 / (k_{\parallel}^2 v_{\text{th}}^2)$, one sees that this condition is exactly the same as Eq. (16). The proper account of ion sound wave coupling for $T_i \sim T_e$ is difficult because ion FLR effects are *not* negligible in this case, since ρ_s (the main scale-length of the ion motion) is comparable to ρ_i .

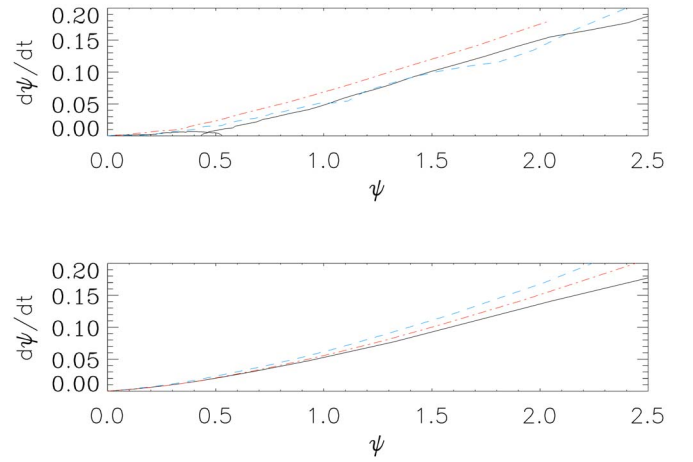


FIG. 5. (Color online) Gyrokinetic (upper panel) and two-fluid (lower panel) nonlinear reconnection rates for case II vs ψ , the reconnected flux inside the island, for $T_i \leq T_e$ (solid line), $T_i = T_e$ (dotted-dashed), $T_i = 5T_e$ (dashed).

In the case of the perpendicular ion dynamics, the importance of ion FLR effects has long been appreciated and was first studied in detail in Ref. 10. This work, like the calculations presented in Appendix B, is based on a Padé approximation of the perpendicular kinetic ion response that is leading-order accurate in the limits of both $k_{\perp} \rho_i \gg 1$ and $k_{\perp} \rho_i \rightarrow 0$. In view of the role of ion FLR effects in these calculations, it is perhaps surprising that the resulting dispersion relation [Eq. (B19)] for arbitrary T_i/T_e may also be obtained from various two-fluid calculations^{12,16,17,19,20} in the limit that isothermal electron and ion fluid equations of state are used. The reason for this agreement, as we show in Appendix B, is that the Padé approximation to the perpendicular kinetic ion response is exactly reproduced by the usual low-frequency, reduced-MHD-type approach provided that the ion diamagnetic drift is properly included. The numerical solution to the four coupled reduced two-fluid equations discussed in Ref. 12, shown in Figs. 1 and 2 as the upper ($T_i/T_e=5$) and lower ($T_i=0$) solid lines, go beyond Eqs. (10) and (11) to include in the zero-FLR limit ion-sound-wave coupling and finite β effects. While both of these effects are stabilizing, the fluid predictions for $T_i=5T_e$ are still substantially larger than the GS2 values, indicating the kinetic effects discussed earlier are important.

IV. NONLINEAR REGIME

Turning now to the nonlinear evolution, we again consider the parameters of case II discussed in Sec. III. As noted earlier the nonlinear runs have a box size $L_y=2.5L_x$, corresponding to $k_{y \text{ min}} \rho_{se}=0.08$. This minimum k_y corresponds roughly to the fastest growing linear mode. Following the initialization of the run with small amplitude random noise, this longest-wavelength mode dominates the system as the nonlinear phase is reached. Because this mode falls within in the large Δ' regime, the simulations discussed here, aside from the guide field, are similar to those of the GEM Reconnection Challenge Project.⁵

Figure 5 shows the nonlinear reconnection rates $d\psi/dt$

for case II as a function of ψ , the reconnected flux inside the magnetic island. The upper panel shows the GS2 values for $T_i \ll T_e$ (solid line), $T_i = T_e$ (dotted-dashed), $T_i = 5T_e$ (dashed). The nonmonotonic feature in the curve for $T_i/T_e \ll 1$ near $\psi \approx 0.5$ is due to the initial noise in the system, which at early times leads to competition between the dominant mode with $k_y \rho_{se} = 0.08$ and the next-order harmonic. Here ψ is normalized to $B_{0,\max} d_i$ and t to γ_A . At the final times shown in the figure the island widths are roughly half the box size $w \sim L_x/2$. In all three cases the reconnection continues until the islands span the entire box ($w \sim L_x$), although the reconnection rates drop sharply at times just beyond those shown in the figure. The lower panel shows the analogous results obtained from a simple isothermal two-fluid simulation with the same parameters and a large guide field ($B_z \approx 10B_{x,\max}$). The generalized Ohm's law in this model includes the Hall terms and electron inertia.⁵ The reconnection rates in the gyrokinetic system are comparable to those in the fluid model and, like the linear gyrokinetic growth rates, exhibit little dependence on T_i/T_e . Numerical tests also show the contribution of \tilde{B}_\parallel in the gyrokinetic equations (see Appendix A) to both the linear and nonlinear reconnection rates is small ($\leq 5\%$), in contrast to what one might expect for the higher T_i cases in which $\beta \sim \beta_i \sim 1$.

The fluid code used here was benchmarked in the GEM reconnection study⁵ against full-particle simulations and was found to produce similar rates of reconnection. Subsequent work with this same fluid code was carried out, e.g. in Ref. 21, that explored the dependence of the reconnection rate on the guide field strength, the plasma β , and other parameters. In the strong guide field regime with $\rho_s > d_e$ relevant to our simulations, the reconnection rates were characterized by inflow velocities that scale roughly as a small fraction (~ 0.05) of the Alfvén speed based on the reconnecting component of the magnetic field just upstream of the reconnection region,

$$V_{\text{in}} \sim \frac{\delta}{l} V_{\text{out}} \sim 0.05 V_{\text{out}}, \quad V_{\text{out}} \sim \frac{B_{y,\text{up}}}{\sqrt{4\pi n m_i}}. \quad (17)$$

Similar rates have also been observed²² in particle simulations of strong guide field reconnection with a realistic mass ratio, $m_i/m_e = 1836$.

In the present system, the reconnecting component of the magnetic field near the reconnection layer is given by

$$B_{y0}(x) = B_{y0 \max} \sin(k_x x) \approx B'_{y0} x + \dots, \quad B'_{y0} = k_x B_{y0 \max} \quad (18)$$

or in terms of the flux function ($B_y = \partial\psi/\partial x$):

$$\psi \approx \frac{1}{2} B'_{y0} x^2. \quad (19)$$

As reconnection proceeds in the nonlinear phase, the flux surfaces upstream of the reconnection layer at $x=0$ are shifted toward the layer, causing an increase in the local values of B_y and ψ . Denoting this time dependent shift in the x direction by $\xi(t)$, the values of B_y and ψ just upstream of the layer at $x=0$ can be estimated by replacing $x \rightarrow \xi$ in the equilibrium profiles,

$$B_{y,\text{up}} \approx B'_{y0} \xi, \quad \psi \approx \frac{1}{2} B'_{y0} \xi^2. \quad (20)$$

From the expression for ψ one finds

$$\frac{1}{\psi} \frac{d\psi}{dt} = \frac{2}{\xi} \frac{d\xi}{dt}. \quad (21)$$

An expression for $d\xi/dt$ may be obtained from the continuity equation as

$$\frac{d\xi}{dt} = V_{\text{in}} = \frac{\delta}{l} V_{\text{out}}, \quad V_{\text{out}} \sim \frac{B_{y,\text{up}}}{\sqrt{4\pi n m_i}}, \quad B_{y,\text{up}} = B'_{y0} \xi \quad (22)$$

or equivalently,

$$\frac{d\xi}{dt} = \frac{\delta}{l} \frac{B'_{y0}}{\sqrt{4\pi n m_i}} \xi. \quad (23)$$

Equation (21) can thus be written as

$$\frac{1}{\psi} \frac{d\psi}{dt} = \frac{2}{\xi} \frac{d\xi}{dt} = \frac{2\delta}{l} \frac{B'_{y0}}{\sqrt{4\pi n m_i}} = \frac{2\delta}{l} k_x V_{Ay}. \quad (24)$$

Estimating $\delta/l \sim 0.05$ and normalizing the time units to γ_A as in Fig. 5, this expression reduces to

$$\frac{d\psi}{dt} = \frac{2\delta}{l} \gamma_A \psi \approx 0.1 \psi. \quad (25)$$

One would therefore expect the slopes of the curves in Fig. 5 at early times to be constant and roughly equal to 0.1, which indeed they are. The constancy of the slope implies that the reconnected flux and magnetic island width grow exponentially with time.

Concerning the insensitivity of the gyrokinetic system to T_i/T_e , a caveat must be added regarding the level of noise that is initially imposed on the simulations. The solid curve in Fig. 6 shows the island width as a function of time in the $T_i = 5T_e$ simulation shown in Fig. 5 (top panel). The initial noise level in this simulation is small but finite, such that values of w smaller than about $w \sim 0.01 \rho_{se}$ (the starting value of the solid curve) cannot be distinguished from the initial noise. The island width in this case does not saturate and reconnection continues until essentially all the flux in the

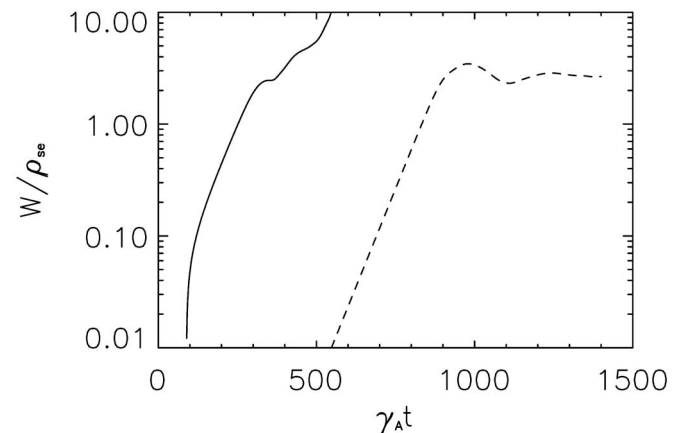


FIG. 6. Island widths w/ρ_{se} vs $\gamma_A t$ for $T_i/T_e = 5$ with (solid) and without (dashed) added initial noise in the simulation. The nonlinear saturation is avoided for very weak levels of initial noise.

system is reconnected. When the noise level is drastically reduced (dashed curve), however, the growth of the island halts at about $w \sim 2\rho_{se} \sim \rho_i$. Apparently the saturation mechanism, at least for these parameters, is fragile and easily destroyed by the presence of noise in the system—a feature that may explain why such saturation behavior has not been previously observed in particle simulations of similar large-guide-field systems (see, e.g., Ref. 23). Such early nonlinear saturation is not observed in the fluid simulation of the same system, or in the gyrokinetic simulations at smaller T_i/T_e .

Saturation behavior superficially similar to that observed here has been reported in one particle simulation study²⁴ of reconnection in a high-beta system without a guide field. It was conjectured the saturation was due to the formation of electron temperature anisotropies ($T_{e\perp} < T_{e\parallel}$), which are known to have a potentially strong stabilizing impact on the reconnection. In our system the initial plasma equilibrium is isotropic and in the strong guide-field limit the perturbations of the plasma temperatures, densities, and pressures are small (see, e.g., Ref. 25 for discussion). On the theoretical side, the saturation of tearing modes has been studied in both low and high β plasmas (e.g., Refs. 26–28). Consistent with our findings, in Ref. 28 nonlinear saturation in the strong guide field regime is predicted when $w \sim \rho_i$ due to the interaction of the ions with the electrostatic field of the reconnecting mode (ion trapping). This study, however, considers systems in which an ambient pressure gradient (absent in the system considered here) leads to a real-frequency of the mode (also absent here) that is larger than the linear growth rate. Further study of this issue is needed, therefore, to determine if the physical mechanism described in that work is consistent with our simulations.

V. CONCLUSION

We have explored linear and nonlinear collisionless reconnection in the $\rho_s > d_e$ regime using gyrokinetic simulations. In the linear-theory limit, the gyrokinetic growth rates are compared to analytic calculations across a range of parameters, including small and large Δ' and T_i/T_e . For the cases in which the analytic calculations of the growth rate are theoretically reliable for our parameters (low β and small T_i/T_e), reasonably good agreement between the theory and simulations is found, while for some other cases ($\beta \sim 1$ and $T_i \gtrsim T_e$), further analytic work is needed to provide a sound benchmark for the simulations. In particular, the insensitivity of the linear growth rates in the gyrokinetic model to T_i/T_e and the plasma β , apparently due to the role played by FLR effects in the parameter regimes considered here, are not well reproduced by existing analytic calculations. In the nonlinear regime, the reconnection rates at large Δ' were explored for various values of T_i/T_e , and found to be similar to those obtained from a two-fluid model. As in the linear case, the dependence of the nonlinear reconnection rates on T_i/T_e is quite weak. An exception to this occurs at larger T_i/T_e ($T_i/T_e = 5$) and very weak initial perturbations, in which the growth of the island width in the gyrokinetic system

saturates at the ρ_i -scale. This saturation for our parameters may be overcome by adding small levels of initial noise to the simulations.

ACKNOWLEDGMENTS

This material is based upon work supported by NSF Grant No. 0238694, the Center for Multiscale Plasma Dynamics, and DOE Grant No. DE-FC02-04ER54784. P.R. is supported by a EURATOM Fusion fellowship.

APPENDIX A: THE GS2 GYROKINETIC EQUATIONS

The gyrokinetic equations, with species label α , may be written as³

$$\begin{aligned} & \left(\frac{\partial}{\partial t} + i\Omega_{d\alpha} + v_{\parallel} \nabla_{\parallel} \right) h_{\alpha}(\mathbf{k}_{\perp}) + \frac{c}{4\pi^2 B} \\ & \times \sum_{\mathbf{k}'_{\perp}, \mathbf{k}''_{\perp}} [\mathbf{b} \cdot (\mathbf{k}'_{\perp} \times \mathbf{k}''_{\perp})] \cdot \chi(\mathbf{k}'_{\perp}) h_{\alpha}(\mathbf{k}''_{\perp}) \delta_{\mathbf{k}'_{\perp} + \mathbf{k}''_{\perp}, \mathbf{k}_{\perp}} \\ & = - \left(\frac{\partial}{\partial t} + i\Omega_{* \alpha} \right) \chi(\mathbf{k}_{\perp}) q_{\alpha} \frac{\partial F_{0\alpha}}{\partial \epsilon} \\ & + \frac{1}{2\pi} \int_{-\pi}^{\pi} \exp(-iL) C(f_{\alpha}) d\xi, \end{aligned} \quad (\text{A1})$$

where $L = (\mathbf{v} \times \mathbf{b} \cdot \mathbf{k}_{\perp}) / \Omega_{c\alpha}$, ξ is the gyroangle, $\epsilon = m_{\alpha} v^2 / 2$ is the particle energy, $\mu = m_{\alpha} v_{\perp}^2 / 2B$ is the magnetic moment, χ is the generalized gyrokinetic potential

$$\chi = J_0 \left(\frac{k_{\perp} v_{\perp}}{\Omega_{c\alpha}} \right) \left(\phi - \frac{v_{\parallel}}{c} A_{\parallel} \right) + J_1 \left(\frac{k_{\perp} v_{\perp}}{\Omega_{c\alpha}} \right) \frac{v_{\perp}}{k_{\perp} c} \delta B_{\parallel}, \quad (\text{A2})$$

ϕ is the electrostatic potential, A_{\parallel} is the parallel component of the vector potential, δB_{\parallel} is the perturbation of the parallel magnetic field, \mathbf{b} is the magnetic-field unit vector, $\delta_{\mathbf{k}'', \mathbf{k}'} = 0$ for $\mathbf{k}'' \neq \mathbf{k}'$ and $\delta_{\mathbf{k}'', \mathbf{k}'} = 1$ for $\mathbf{k}'' = \mathbf{k}'$, $\Omega_{c\alpha} = q_{\alpha} B_{\theta} / (m_{\alpha} c)$, and $C(f_{\alpha})$ is a collision operator (not relevant to the present work). The nonadiabatic part of the distribution function $h_{\alpha} = h_{\alpha}(\epsilon, \mu, t)$ is related to the total perturbed distribution function $f_{\alpha} = f_{\alpha}(\mathbf{v}, t)$ through $f_{\alpha} = q_{\alpha} \phi \partial F_{0\alpha} / \partial \epsilon + \exp(iL) h_{\alpha}$, or $\langle f_{\alpha} \rangle_{\xi} = q_{\alpha} \phi \partial F_{0\alpha} / \partial \epsilon + J_0 h_{\alpha}$. The frequencies $\Omega_{d\alpha}$ and $\Omega_{* \alpha}$ are defined as

$$\Omega_{* \alpha} = \frac{\mathbf{b} \times \mathbf{k}_{\perp} \cdot \nabla F_{0\alpha}}{m_{\alpha} \Omega_{c\alpha} \partial F_{0\alpha} / \partial \epsilon}, \quad (\text{A3})$$

$$\Omega_{d\alpha} = \mathbf{k}_{\perp} \cdot \mathbf{b} \times \frac{m_{\alpha} v_{\parallel}^2 \mathbf{b} \cdot \nabla \mathbf{b} + \mu \nabla B}{m_{\alpha} \Omega_{c\alpha}}. \quad (\text{A4})$$

The ion and electron “background” distribution functions $F_{0\alpha}$ are assumed to be isotropic Maxwellians. The gyrokinetic equations are coupled to the Maxwell equations, which may be written as

$$\sum_{\alpha} \int d^3 v q_{\alpha} \left[q_{\alpha} \phi \frac{\partial F_0}{\partial \epsilon} + J_0 h_{\alpha} \right] = 0, \quad (\text{A5})$$

$$\nabla_{\perp}^2 A_{\parallel} = - \frac{4\pi}{c} \sum_{\alpha} \int d^3 v q_{\alpha} v_{\parallel} J_0 h_{\alpha}, \quad (\text{A6})$$

$$\delta B_{\parallel} = -\frac{4\pi}{c} \sum_{\alpha} \int d^3v \frac{q_{\alpha} v_{\perp}}{k_{\perp}} J_1 h_{\alpha}. \quad (\text{A7})$$

APPENDIX B: LINEAR THEORY

Assuming $\gamma \gg k_{\parallel} c_s$, the ion density perturbation \tilde{n}_i is given by (see, e.g., Ref. 10)

$$\tilde{n}_i = \frac{n_0 e}{T_i} [\Gamma_0(b) - 1] \phi, \quad \Gamma_0(b) = I_0(b) e^{-b}, \quad b = -\rho_i^2 \nabla_{\perp}^2, \quad (\text{B1})$$

where $\rho_i = \sqrt{T_i/m_i}/\Omega_{ci}$ is the ion Larmor radius and I_0 is the modified Bessel function. The perturbed electron continuity equation gives

$$\tilde{n}_e \simeq \frac{1}{\gamma e} \nabla_{\parallel} \tilde{J}_{\parallel} = x \frac{c^2 k_{\parallel}'^2}{4\pi e \gamma^2} A'', \quad A = \frac{\gamma}{ik_{\parallel}' c} A_z, \quad (\text{B2})$$

where in the linear regime we have assumed

$$\nabla_{\parallel} = ik_{\parallel}' x, \quad k_{\parallel}' = \frac{k_y}{B_{z0}} \left[\frac{dB_{y0}}{dx} \right]_{x=0} = \frac{k_y \gamma_A}{V_A}, \quad \tilde{J}_{\parallel} \simeq -\frac{c}{4\pi} A_z''. \quad (\text{B3})$$

The quasineutrality condition $\tilde{n}_i = \tilde{n}_e$ can thus be written as

$$\frac{T_e}{T_i} [\Gamma_0 - 1] \phi = x \frac{k_y^2 \rho_{se}^2 \gamma_A^2}{\gamma^2} A''. \quad (\text{B4})$$

Finally, the generalized Ohm's law, assuming an isothermal electron response, is

$$-\frac{m_e \gamma}{e} \tilde{J}_{\parallel} = -\nabla_{\parallel} (T_e \tilde{n}_e) - n_0 e E_{\parallel} \quad (\text{B5})$$

or equivalently, using Eqs. (B2) and (B3)

$$-\frac{E_{\parallel}}{ik_{\parallel}'} = x\phi + A = \frac{k_y^2 \rho_{se}^2 \gamma_A^2}{\gamma^2} (\delta_e^2 + x^2) A'', \quad (\text{B6})$$

$$\delta_e^2 = \frac{\gamma^2}{k_{\parallel}'^2 v_{the}^2},$$

$$v_{the}^2 = \frac{T_e}{m_e}.$$

To make progress, we introduce the auxiliary variable ϕ_i defined as

$$\frac{T_e}{T_i} [\Gamma_0 - 1] \phi \equiv \rho_{se}^2 \nabla_{\perp}^2 \phi_i \quad (\text{B7})$$

or equivalently,

$$\phi = \frac{\rho_i^2 \nabla_{\perp}^2}{[\Gamma_0 - 1]} \phi_i. \quad (\text{B8})$$

We demonstrate below that $c\phi_i/B$ is the ion velocity stream function in two-fluid theory. Now making the well-known Padé approximation

$$\Gamma_0 \simeq \frac{1}{1 - \rho_i^2 \nabla_{\perp}^2}, \quad (\text{B9})$$

Eq. (B8) simply becomes

$$\phi = (1 - \rho_i^2 \nabla_{\perp}^2) \phi_i. \quad (\text{B10})$$

Eliminating ϕ in Eqs. (B4) and (B6) with Eqs. (B7) and (B10), respectively, one obtains

$$\phi_i'' = x \frac{k_y^2 \gamma_A^2}{\gamma^2} A'' = \frac{k_y^2 \gamma_A^2}{\gamma^2} \partial_x [x^2 \partial_x (A/x)], \quad (\text{B11})$$

$$x\phi_i + A = \frac{k_y^2 \rho_s^2 \gamma_A^2}{\gamma^2} (\delta^2 + x^2) A'', \quad \delta^2 = \frac{\delta_e^2}{1 + T_i/T_e}. \quad (\text{B12})$$

Note that the contribution of the $\rho_i^2 \partial_x^2$ terms arising from Eq. (B10) has simply led to the replacements $\delta_e \rightarrow \delta$, $\rho_{se} \rightarrow \rho_s$ in Ohm's law, or equivalently, $T_e \rightarrow T_e + T_i$. The solutions for ϕ_i and A for $x \rightarrow +\infty$ must be matched to the asymptotic forms

$$\phi_i \simeq \phi_{\infty} = \text{const}, \quad A \simeq -\phi_{\infty} (x + 2/\Delta'). \quad (\text{B13})$$

With this boundary condition, Eq. (B11) may be integrated from $x=0$ to $x=\infty$ to yield the constraint

$$-\phi_i'(0) = \frac{k_y^2 \gamma_A^2}{\gamma^2} \left(\frac{2\phi_{\infty}}{\Delta'} + A(0) \right). \quad (\text{B14})$$

The constants in this expression may be related to each other from the solution to Eqs. (B11) and (B12). Assuming $\rho_s > d_e$, this solution, discussed for example in Ref. 20, turns out to have two scales: an inner scale δ that determines the width of the current profile (i.e., A''), and an outer scale ρ_s that determines the behavior of ϕ_i . On the inner scale, the ϕ_i term in Eq. (B12) can be neglected and one can take $A = A_0 + A_1 + \dots$, where $A_0 = A(0)$ is a constant (that is, the constant ψ approximation is valid), yielding

$$A'' = A_1'' \simeq \Gamma^2 \frac{A_0}{(\delta^2 + x^2)}, \quad \Gamma = \frac{\gamma}{k_y \rho_s \gamma_A}. \quad (\text{B15})$$

Integrating this expression and comparing it to Eq. (B13) for $x \gg \delta$ one obtains

$$A' \simeq \Gamma^2 \frac{A_0}{\delta} \tan^{-1}(x/\delta) = -\phi_{\infty} \frac{2}{\pi} \tan^{-1}(x/\delta). \quad (\text{B16})$$

In the outer region $x \gg \delta$, one can neglect the δ^2 term in Eq. (B12) and eliminate A'' with Eq. (B11), yielding

$$x\phi_i + A = x\rho_s^2 \phi_i''. \quad (\text{B17})$$

Differentiating this equation with respect to x , using $A' \simeq -\phi_{\infty}$, and noting $\phi_i(0) = 0$, one finds the solution

$$\phi_i \simeq \phi_{\infty} (1 - e^{-x/\rho_s}). \quad (\text{B18})$$

Finally, returning to Eq. (B14) with this solution, and using [from Eq. (B16)] $A(0) = -2\delta\phi_{\infty}/(\Gamma^2\pi) = -2d_e\phi_{\infty}/(\Gamma\pi)$, one obtains the dispersion relation

$$\Gamma^3 = \frac{\gamma^3}{k_y^3 \rho_s^3 \gamma_A^3} = \frac{2 d_e}{\pi \rho_s} \left(1 - \frac{\Gamma \pi}{d_e \Delta'} \right). \quad (\text{B19})$$

At $\Delta' \rightarrow \infty$ this reduces to Eq. (10) while at small Δ' , neglecting the left-hand side, it reduces to Eq. (11).

1. Parallel electric field E_{\parallel}

From Eq. (B6), the parallel electric field is given by

$$E_{\parallel} = -ik'_{\parallel}(x\phi + A) = -ik'_{\parallel} \frac{k_y^2 \rho_{se}^2 \gamma_A^2}{\gamma^2} (\delta_e^2 + x^2) A''. \quad (\text{B20})$$

In the inner zone $x \ll \rho_s$, the approximate solution for A'' is given by Eq. (B15),

$$E_{\parallel} \approx -ik'_{\parallel} \left(\frac{\delta_e^2 + x^2}{\delta^2 + x^2} \right) \frac{A_0}{1 + T_i/T_e} = E_{\parallel}(0) \left(\frac{\delta^2 + \frac{T_e}{T_e + T_i} x^2}{\delta^2 + x^2} \right). \quad (\text{B21})$$

In the outer zone $x \sim \rho_s$, one may use Eq. (B11) to express A'' in terms of ϕ''_i , and then use the expression for ϕ_i given by Eq. (B18),

$$E_{\parallel} = -ik'_{\parallel} x \left(\frac{\delta_e^2 + x^2}{x^2} \right) \rho_{se}^2 \phi''_i \approx ik'_{\parallel} x \left(\frac{\delta^2 + \frac{T_e}{T_e + T_i} x^2}{x^2} \right) \phi_{\infty} e^{-x/\rho_s}. \quad (\text{B22})$$

2. Ion velocity stream function ϕ_i

Here we show the variable ϕ_i as defined by Eq. (B10) is proportional to the ion velocity stream function in two fluid theory. With this interpretation Eq. (B11) becomes, both physically and mathematically, the ion vorticity equation of the fluid model. Since Eqs. (B10) and (B11) were constructed to be accurate (to leading order) for $\rho_i^2 \nabla_{\perp}^2 \gg 1$ as well as $\rho_i^2 \nabla_{\perp}^2 \rightarrow 0$, this accounts for why the two-fluid model yields a correct representation of ion FLR effects in the former limit.

Operating on the ion momentum equation with $\vec{B} \times$, assuming an isothermal ion equation of state, and considering linear perturbations yields

$$\vec{v}_{i\perp} \approx \frac{c}{B} \hat{z} \times \nabla_{\perp} \Phi + \frac{1}{\Omega_{ci}} \frac{\partial}{\partial t} \hat{z} \times \vec{v}_{i\perp}, \quad (\text{B23})$$

where

$$\Phi = \phi + \frac{T_i}{n_0 e} \tilde{n}. \quad (\text{B24})$$

Here Φ , aside from a constant factor of c/B , is the ion velocity stream function and with Eq. (B10) we will show in a moment that $\Phi = \phi_i$. For $\partial/\partial t \ll \Omega_{ci}$ the second term on the right-hand side of Eq. (B23) is small compared to the first, leading to the iterative solution

$$\vec{v}_{i\perp} \approx \frac{c}{B} \left(\hat{z} \times \nabla_{\perp} \Phi - \frac{1}{\Omega_{ci}} \frac{\partial}{\partial t} \nabla_{\perp} \Phi \right). \quad (\text{B25})$$

Substituting this into the linearized ion continuity equation and neglecting the parallel ion motion yields

$$\frac{\partial}{\partial t} \tilde{n} \approx n_0 \nabla_{\perp} \cdot \vec{v}_{i\perp} = \frac{n_0 c}{B \Omega_{ci}} \frac{\partial}{\partial t} \nabla_{\perp}^2 \Phi \quad (\text{B26})$$

or

$$\tilde{n} = \frac{n_0 c}{B \Omega_{ci}} \nabla_{\perp}^2 \Phi. \quad (\text{B27})$$

Substituting this into Eq. (B24) yields $\Phi = \phi + \rho_i^2 \nabla_{\perp}^2 \Phi$ or equivalently,

$$\phi = \Phi - \rho_i^2 \nabla_{\perp}^2 \Phi. \quad (\text{B28})$$

Comparing this to Eq. (B10) one sees that $\Phi = \phi_i$ as claimed.

3. Electron drift kinetic treatment

The electrons satisfy the drift kinetic equation,

$$\frac{d}{dt} \tilde{f} + \frac{c}{B \Omega_{ce}} f_0 \frac{d}{dt} \nabla_{\perp}^2 \phi = \frac{e}{m_e} \frac{\partial f_0}{\partial v_{\parallel}} E_{\parallel}, \quad \frac{d}{dt} = \frac{\partial}{\partial t} + v_{\parallel} \nabla_{\parallel}, \quad (\text{B29})$$

where $f = f_0 + \tilde{f}$, $E_{\parallel} = -\nabla_{\parallel} \phi - \partial A_z / \partial t$, and the second term arises from the polarization drift,

$$\nabla_{\perp} \cdot \vec{v}_p f \approx \frac{c}{B \Omega_{ce}} f_0 \frac{d}{dt} \nabla_{\perp}^2 \phi. \quad (\text{B30})$$

Defining $\rho_e = v_{the} / \Omega_{ce}$, $v_{the} = \sqrt{T_e / m_e}$, $\Omega_{ce} = eB / (m_e c)$, assuming

$$f_0 \approx \frac{n_0}{(2\pi)^{3/2} v_{the}^3} \exp[-(v_{\perp}^2 + v_{\parallel}^2) / (2v_{the}^2)] \quad (\text{B31})$$

and taking for linear perturbations $\nabla_{\parallel} = ik'_{\parallel} x$, $\partial/\partial t = \gamma$, Eq. (B29) yields

$$\tilde{f} = -\frac{ef_0}{T_e} \frac{v_{\parallel}}{\gamma + ik'_{\parallel} x v_{\parallel}} E_{\parallel} - \frac{cf_0}{B \Omega_{ce}} \nabla_{\perp}^2 \phi. \quad (\text{B32})$$

With this expression, the electron density may be written as

$$\tilde{n}_e = \int d^3 v \tilde{f} = -(1-I) \frac{en_0}{T_e} \frac{E_{\parallel}}{ik'_{\parallel} x} - \frac{en_0}{T_e} \rho_e^2 \nabla_{\perp}^2 \phi, \quad (\text{B33})$$

where

$$I = \frac{1}{\sqrt{2\pi} v_{the}} \int_{-\infty}^{\infty} dv_{\parallel} \frac{e^{-v_{\parallel}^2 / (2v_{the}^2)}}{1 + ik'_{\parallel} x v_{\parallel} / \gamma} = \frac{2}{\sqrt{\pi}} \int_0^{\infty} dz \frac{e^{-z^2}}{1 + \alpha^2 z^2}, \quad \alpha = \sqrt{2} \frac{x}{\delta_e}. \quad (\text{B34})$$

Noting that $I \approx \sqrt{\pi} / \alpha$ for $\alpha \rightarrow \infty$ and $I \approx 1 - \alpha^2 / 2$ for $\alpha \rightarrow 0$, one is led to the Padé approximation for $1 - I$,

$$1 - I \approx \frac{x^2}{x^2 + \delta_e^2} \quad (\text{B35})$$

with which Eq. (B33) can be written as

$$\tilde{n}_e = -\frac{en_0}{T_e} \left(\frac{x^2}{x^2 + \delta_e^2} \frac{E_{\parallel}}{ik'_{\parallel} x} + \rho_e^2 \nabla^2 \phi \right). \quad (\text{B36})$$

If one neglects the ρ_e^2 term on the right-hand side, this equation becomes identical to Ohm's law, Eq. (B5), if one expresses \tilde{J}_{\parallel} on the left-hand side of Eq. (B5) in terms of \tilde{n}_e using Eq. (B2). Continuing, setting $\tilde{n}_i = \tilde{n}_e$ with \tilde{n}_i given by Eq. (B1) one finds

$$\left(\frac{x^2}{x^2 + \delta_e^2} \right) (x\phi + A) = \frac{T_e}{T_i} [\Gamma_0 - 1] \phi + \rho_e^2 \phi'' \quad (\text{B37})$$

or using Eq. (B9) to eliminate ϕ and rearranging terms,

$$x(x\phi + A) = (x^2 + \delta_e^2) \rho_s^2 \phi_i'' - \rho_e^2 \rho_i^2 (x^2 + \delta_e^2) \phi_i'''' . \quad (\text{B38})$$

If one neglects the electron polarization drift term $\propto \rho_e^2$ on the right-hand side and uses Eq. (B11), this equation reduces to Eq. (B12). Estimating $\phi_i'''' \sim \phi_i'' / \delta^2$ (valid if the ρ_e^2 term is small) one sees that the ratio of the ϕ_i'''' term to the ϕ_i'' term in Eq. (B38) for $x \sim \delta$ is $(T_i/T_e) \rho_e^2 / \delta^2$. The same conclusion follows from Eq. (B37), neglecting Γ_0 under the assumption $\delta \ll \rho_i$.

¹M. Kotschenreuther, G. Rewoldt, and W. M. Tang, *Comput. Phys. Commun.* **88**, 128 (1995).

²W. Dorland, F. Jenko, M. Kotschenreuther, and B. N. Rogers, *Phys. Rev. Lett.* **85**, 5579 (2000).

³E. A. Frieman and L. Chen, *Phys. Fluids* **25**, 502 (1982).

⁴M. A. Beer, S. C. Cowley, and G. W. Hammett, *Phys. Plasmas* **2**, 2687 (1995).

⁵J. Birn, R. E. Denton, J. F. Drake, B. N. Rogers, M. A. Shay, M. Hesse, M. Kuznetsova, Z. W. Ma, and A. Bhattacharjee, *J. Geophys. Res.* **106**, 3715, DOI: 10.1029/1999JA900449 (2001).

⁶R. Sydora, *Phys. Plasmas* **9**, 1929 (2001).

⁷W. Wan, Y. Chen, and S. Parker, *IEEE Trans. Plasma Sci.* **33**, 609 (2005).

⁸W. Wan, Y. Chen, and S. Parker, *Phys. Plasmas* **12**, 012311 (2005).

⁹H. Furth, J. Killeen, and M. Rosenbluth, *Phys. Fluids* **6**, 459 (1963).

¹⁰F. Porcelli, *Phys. Rev. Lett.* **66**, 425 (1991).

¹¹J. Drake, *Phys. Fluids* **21**, 1777 (1978).

¹²R. Fitzpatrick and F. Porcelli, *Phys. Plasmas* **14**, 049902 (2007).

¹³D. Grasso, M. Ottaviani, and F. Porcelli, *Nucl. Fusion* **42**, 1067 (2002).

¹⁴G. Laval, R. Pellat, and M. Vuillemin, *Plasma Physics and Controlled Nuclear Fusion Research* (IAEA, Vienna, 1965), Vol. II, p. 259.

¹⁵J. Drake and Y. Lee, *Phys. Fluids* **2**, 1341 (1977).

¹⁶V. Mirmov, C. C. Hegna, and S. Prager, *Phys. Plasmas* **11**, 4468 (2004).

¹⁷R. Fitzpatrick and F. Porcelli, *Phys. Plasmas* **11**, 4713 (2004).

¹⁸J. Drake and M. Shay, "The fundamentals of collisionless reconnection" in *Reconnection of Magnetic Fields: Magnetohydrodynamic and Collisionless Theory and Observations*, edited by J. Birn and E. R. Priest (Cambridge University Press, Cambridge, 2007), Chap. 3.1.

¹⁹A. Y. Aydemir, *Phys. Fluids* **27**, 2877 (1981).

²⁰L. Zakharov and B. Rogers, *Phys. Fluids B* **4**, 3285 (1992).

²¹B. N. Rogers, R. E. Denton, J. F. Drake, and M. A. Shay, *Phys. Rev. Lett.* **87**, 195004 (2001).

²²P. Ricci, J. Brackbill, W. Daughton, and G. Lapenta, *Phys. Plasmas* **11**, 4102 (2004).

²³P. L. Prichett, *Phys. Plasmas* **12**, 062301 (2005).

²⁴P. Ricci, J. Brackbill, W. Daughton, and G. Lapenta, *Phys. Plasmas* **11**, 4489 (2004).

²⁵B. N. Rogers, R. E. Denton, and J. F. Drake, *J. Geophys. Res.* **108**, 1111, DOI:10.1029/2002JA009699 (2003).

²⁶D. Biskamp, R. Sagdeev, and K. Shindler, *Cosm. Electrodyn.* **1**, 297 (1970).

²⁷J. Drake and Y. Lee, *Phys. Rev. Lett.* **39**, 453 (1977).

²⁸M. Kuznetsova and L. Zelenyi, *Plasma Phys. Controlled Fusion* **32**, 1183 (1990).